Optical Engineering

OpticalEngineering.SPIEDigitalLibrary.org

Bilateral control-based compensation for rotation in imaging in scan imaging systems

Dapeng Tian
Yutang Wang
Fuchao Wang
Yupeng Zhang

SPIE.

Bilateral control-based compensation for rotation in imaging in scan imaging systems

Dapeng Tian,* Yutang Wang, Fuchao Wang, and Yupeng Zhang
Chinese Academy of Sciences, Changchun Institute of Optics, Fine Mechanics and Physics, Key Laboratory of Airborne Optical Imaging and Measurement, No. 3888, Dong-Nan-Hu Road, Changchun, Jilin 130033, China

Abstract. Scan imaging systems rely on the rotation of a mirror to scan an image. The rotation in the resulting image must be compensated to prevent information loss. Satisfactory performance of an imaging system is difficult to achieve when employing the methods of mechanical transmission and unilateral tracking control, especially when the system suffers from nonlinear factors, disturbances, and dynamic uncertainties. This paper proposes a compensation method based on bilateral control derived from the field of haptic robots. A two-loop disturbance observer was designed to guarantee that the dynamic characteristics of the motor are close to those of the nominal model. The controllers were designed on the basis of the small gain theorem. Experiments were conducted for a comparison with the traditional unilateral control-based compensation. The comparison showed a reduction of 99.83% in the L_2 norm of error, which validates the method. The proposed method improves the accuracy of compensation for rotation in imaging, and demonstrates that bilateral control has feasibility for application in various fields, including photogrammetry. [DOI: 10.1117/1.OE.54.12.124104]

Keywords: scan imaging; rotation in imaging; bilateral control; compensation.

Paper 151201 received Sep. 8, 2015; accepted for publication Dec. 1, 2015; published online Dec. 29, 2015.

1 Introduction

High-coverage imaging systems are urgently required for surveying maps, security, prevention of forest fires, and many other applications.[1,2] Because the field of view in a lens is limited, a scan imaging method is usually employed in practice.[3] To obtain high-quality photographs from a relatively long distance, an optical system should have a long focal distance and large aperture, which means that the imaging system has a large size and rotary inertia.[4] Directly rotating the whole imaging system decreases the speed and efficiency of the scanning. Therefore, a 45° scan mirror is always set in front of the lens,[5] and scan imaging is realized by rotating the scan mirror.

However, rotation of the scan mirror leads to a rotation of the scanned image.[6] This rotation decreases the field of view and thus decreases the efficiency of imaging.[7] Moreover, the scanned image must be rotated in reverse direction by using an image processing algorithm. However, interpolation and approximation are usually employed in digital image processing, which causes a loss of information in the original image.[8] Rotation in imaging also decreases the accuracy of positioning of objects in the scanned image.[9]

In traditional scan imaging systems, transmission mechanisms such as gears and belt rollers are widely used to link the motion of the scan mirror and a Dove prism or an imaging detector [charge-coupled diode or complementary metal-oxide semiconductor (CMOS)]. According to the principles of optics, a completely synchronized motion between the scan mirror and the prism or the imaging detector perfectly compensates for the rotation in imaging.[10] However, nonlinear factors such as backlash and dead space in mechanical systems always limit the accuracy of such an approach.

Therefore, direct-drive motors are being employed increasingly more by researchers and engineers to address the problem of rotation in imaging.[11] This approach uses two motors in the scan system. One motor drives the scan mirror to realize circular imaging, and the other one drives the prism or the imaging detector to compensate for the rotation. The compensation is realized by making the motor that drives the prism or the detector track the position response of the scan mirror.[12] However, traditional tracking control is a unilateral control approach. It only makes use of the position responses of the two motors, and the force/torque information is not employed. This lack of information restricts the practical performance.

Extensive investigation and practice have demonstrated that methods from the field of control engineering are a feasible solution for improving the performance of an optical system. For example, the performance of a fast steer mirror and the whole imaging system incorporating it was improved by control method innovations.[13] The proportional–integral–differential algorithm was introduced in the field of image compression, which successfully decreased variations in video quality.[14] These studies suggest that control methods are a potential way for improving the compensation for rotation in imaging.

One such control method, bilateral control, which was proposed in the field of haptic teleoperation robotics, aims to track synchronous position responses.[15] Many researchers have investigated this control method to achieve ideal haptic transmission, including Lawrence who introduced the four-channel bilateral control framework.[16] This method uses

*Address all correspondence to: Dapeng Tian, E-mail: d.tian@ciomp.ac.cn

0091-3286/2015/$25.00 © 2015 SPIE

both local and remote information of position and force/torque in the control of the robot. However, uncertainties in robots, such as those in the resonance characteristics, and the accuracy of force/torque measurement restrict the effect of the method in practice. To improve the performance, a bilateral control framework based on disturbance observer (DOB) and reaction force/torque observer was proposed.[17] Recently, the problem of communication delay has been studied to realize remote haptic transmission.[18,19] In addition, disturbance rejection has been studied to improve the performance of haptic teleoperation based on bilateral control.[20] However, these studies have been limited to the field of haptic teleoperation robotics.

The most salient advantage of bilateral control is that the control algorithm always achieves satisfactory performance in position tracking between two robots/motors even in the presence of external disturbance forces acting on them. In fact, in a scan imaging system, ideal position tracking is difficult to achieve using traditional synchronization control, especially when there are external disturbances. Then, the pertinent question is: "Is it possible to extend bilateral control to the field of optical imaging and realize high-accuracy compensation for rotation in imaging?"

In this paper, we present an approach to compensation for rotation in imaging based on the concept of bilateral control. We employ the scan controllers of each single motor as virtual human operator and environment. A bilateral control algorithm was designed for such a system to guarantee synchronous position responses between the two motors. Moreover, to guarantee practical performance, a two-loop DOB was designed. All the parameters in the bilateral control were designed on the basis of the small gain theorem to guarantee the method's feasibility. High-accuracy compensation for rotation in imaging was realized by applying the bilateral control to an imaging system. This paper demonstrates the value of bilateral control in fields beyond the haptic teleoperation. Experiments were carried out on a real imaging system to validate the proposal.

This paper is organized as follows: Sec. 2 formulates the problem. Then, Sec. 3 proposes the bilateral control-based compensation for rotation in imaging. Section 4 presents a detailed design and analysis, and Sec. 5 describes the experiments. Finally, Sec. 6 concludes the paper.

2 Problem Formulation

Figure 1 shows a scan imaging system. The 45-deg scan mirror rotates about the axis O_0Z_0, which coincides with the optical axis of the lens. The axes O_0X_0 and O_0Y_0 are parallel to the axes O_1X_1 and O_1Y_1 in the image coordinate system and to OX and OY in the photographic scenery coordinate system, respectively.

The law of reflection in three-dimensional space is

$$\mathbf{A}' = (\mathbf{I} - 2\mathbf{N}\mathbf{N}^{\mathrm{T}})\mathbf{A}, \tag{1}$$

where $\mathbf{A}$ and $\mathbf{A}'$ denote the unit vectors of the incident light and reflection light, respectively, and $\mathbf{N}$ is the unit vector of the normal line of the mirror plane. In Fig. 1, the unit vector of the normal line is $\mathbf{N} = [0, -(\sqrt{2}/2), -(\sqrt{2}/2)]^{\mathrm{T}}$ before scanning.

Assume that the vector along the incident light E_0O_0 is $\mathbf{A}_0 = [0, y_{E0}, z_{E0}]^{\mathrm{T}}$ $(y_{E0} > 0, z_{E0} < 0)$. According to Eq. (1), the reflection light is

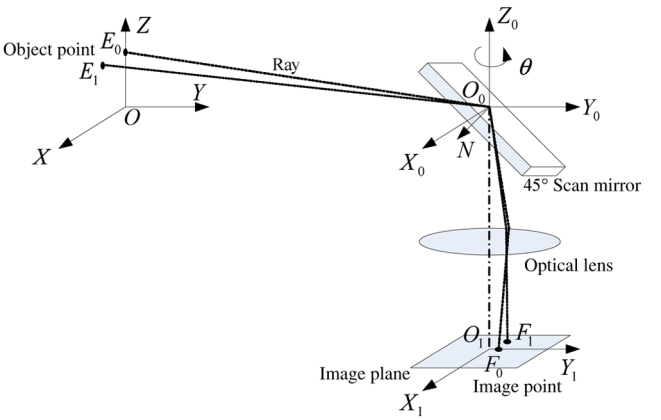

Fig. 1 Image rotation in scan imaging system.

$$\mathbf{A}_0' = [A_{x0}', A_{y0}', A_{z0}']^{\mathrm{T}} = [0, -z_{E0}, -y_{E0}]^{\mathrm{T}}. \tag{2}$$

In the imaging system, the incident light focuses on the image plane through the lens. The coordinates of the image are

$$(x_{F0}, y_{F0}) = \left(-f\frac{A_{x0}'}{A_{z0}'}, -f\frac{A_{y0}'}{A_{z0}'}\right) = \left(0, -f\frac{z_{E0}}{y_{E0}}\right), \tag{3}$$

where f is the focal distance of the lens, which means that the image is located on the axis O_1Y_1.

Assume that the scan mirror rotates by an angle of θ about O_0Z_0 for scanning. In the scan motion, the normal line $\mathbf{N}$ also rotates about the axis O_0Z_0. Then, the coordinates of the rotated normal line $\mathbf{N}'$ are

$$\mathbf{N}' = \begin{bmatrix} \cos\theta & -\sin\theta & 0 \\ \sin\theta & \cos\theta & 0 \\ 0 & 0 & 1 \end{bmatrix} \begin{bmatrix} 0 \\ -\frac{\sqrt{2}}{2} \\ -\frac{\sqrt{2}}{2} \end{bmatrix} = \begin{bmatrix} \frac{\sin\theta}{\sqrt{2}} \\ -\frac{\cos\theta}{\sqrt{2}} \\ -\frac{1}{\sqrt{2}} \end{bmatrix}. \tag{4}$$

The vector of the rotated incident light along E_1O_0 is

$$\mathbf{A} = [\,-y_{E0}\ \sin\theta \quad y_{E0}\ \cos\theta \quad z_{E0}\,]^{\mathrm{T}}. \tag{5}$$

According to Eqs. (1), (4), and (5), the corresponding vector of the reflected light $\mathbf{A}'$ is

$$\begin{bmatrix} A_x' \\ A_y' \\ A_z' \end{bmatrix} = \begin{bmatrix} \cos^2\theta & \sin\theta\cos\theta & \sin\theta \\ \sin\theta\cos\theta & \sin^2\theta & -\cos\theta \\ \sin\theta & -\cos\theta & 0 \end{bmatrix} \begin{bmatrix} -y_{E0}\sin\theta \\ y_{E0}\cos\theta \\ z_{E0} \end{bmatrix} = \begin{bmatrix} z_{E0}\sin\theta \\ -z_{E0}\cos\theta \\ -y_{E0} \end{bmatrix}. \tag{6}$$

After scanning, the coordinates of the image point are

$$(x_{F1}, y_{F1}) = \left(-f\frac{A_x'}{A_z'}, -f\frac{A_y'}{A_z'}\right) = \left(f\frac{z_{E0}\sin\theta}{y_{E0}}, -f\frac{z_{E0}\cos\theta}{y_{E0}}\right). \tag{7}$$

Clearly, the image also rotates about the axis O_0Z_0. The angle of this rotation α is

$$\alpha = \arctan\left(-\frac{x_{F1}}{y_{F1}}\right) = \arctan\left(\frac{\sin\theta}{\cos\theta}\right) = \theta. \quad (8)$$

Therefore, the scan motion of the 45-deg mirror leads to rotation in imaging. To compensate for this rotation, the imaging detector must rotate by the same angle as the scan mirror.[21]

In such a system, two motors are required, one for driving the scan mirror and one for the imaging detector. The objective of this study was to design a control method that makes the error of position tracking between the two motors converge to zero, i.e.,

$$\theta_s(t) - \theta_c(t) \to 0, \qquad (t \to \infty), \quad (9)$$

where θ_s and θ_c denote the position responses of the scan mirror motor and compensation motor, respectively.

3 Bilateral Control-Based Compensation

Assume two virtual operators who turn the scan motor and compensation motor as shown in Fig. 2. Bilateral control for haptic teleoperation guarantees equal angle responses for the two motors regardless of how the virtual operators turn the motors.

The dynamics of the two motors is described as

$$\Theta_i = G_i(s)(U_i + D_i) = \frac{1}{J_{in}s^2 + B_{in}s}[1 + \Delta_i(s)](U_i + D_i) \quad (i = s, c), \quad (10)$$

where J_{in} and B_{in} denote the nominal equivalent rotary inertia and nominal equivalent motor damping coefficient. Θ_i, U_i, and D_i denote the angle response, control input, and equivalent disturbance, respectively, and are the expressions of $\theta_i(t)$, $u_i(t)$, and $d_i(t)$ in the frequency domain. $\Delta(s)$ denotes the dynamic uncertainty. The subscripts s and c represent the scan mirror motor and compensation motor.

Figure 3 illustrates the proposed method of compensation.

In the scan control, a controller provides control values τ_s and τ_c according to the responses of the motors and a scan command. The scan control loops play the roles of two virtual human operators in this system. The scan controller is designed as

$$T_i = C_s(s)(\Theta - \Theta_i) \qquad (i = s, c), \quad (11)$$

where Θ and T_i are the expressions of the scan command θ and torque τ_i in the frequency domain, respectively.

Two robust compensators (Fig. 3) estimate the equivalent disturbances, including external disturbances and uncertainties in the motors, for robust control. The purpose of the robust compensators is to normalize the dynamics from $u'_{xi}(i = s, c)$ to θ_i

$$\Theta_i = \frac{1}{s^2 + \frac{B_{in}}{J_{in}}s} U'_{xi} \qquad (i = s, c). \quad (12)$$

In this study, a two-loop DOB was used as the robust compensator. This method is explained in the next section.

The controllers C_1, C_4, C_s, and C_c are position controllers that are proportional-derivative controllers. The controllers C_2, C_3, C_5, and C_6 are torque controllers that are proportional controllers. The controllers are designed as

$$C_1 = C_4 = C_s = C_c = C_p(s) = K_P + K_D s, \quad (13)$$

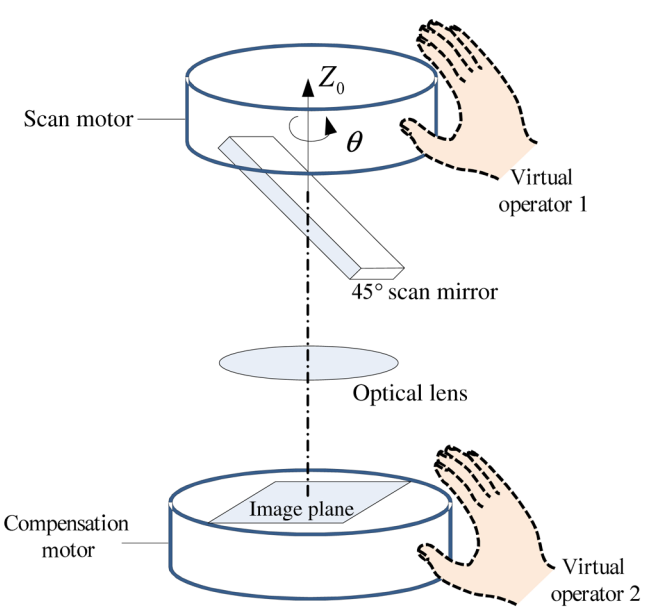

Fig. 2 Scan and compensation imaging system with bilateral control. The scan motor and compensation motor drive the scan mirror and detector, respectively. The controller plays the role of two virtual operators who move two motors.

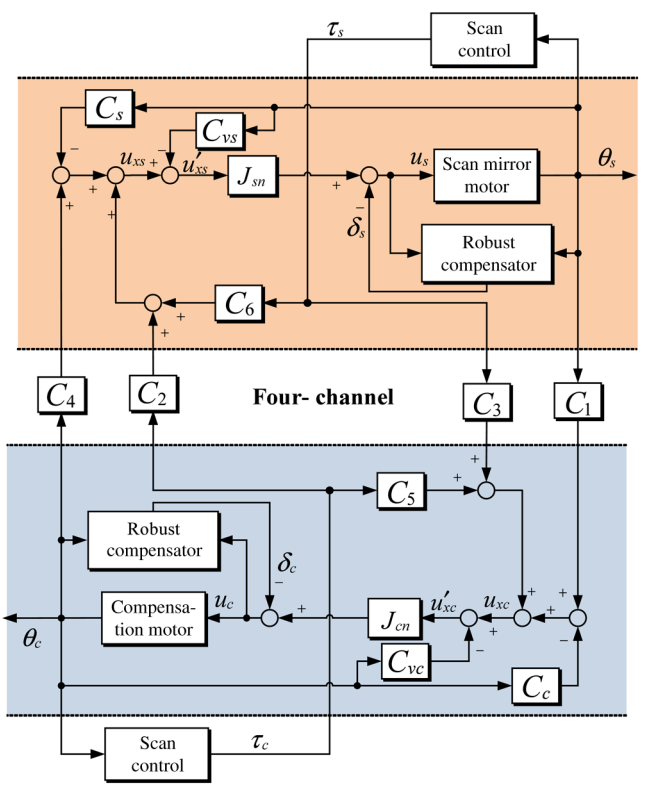

Fig. 3 Compensation for rotation in imaging based on four-channel bilateral control. This control method makes use of both the position and torque information of both motors.

$$C_2 = C_3 = C_5 = C_6 = C_t = K_t, \tag{14}$$

where K_P, K_D, and K_t are the proportional gain, derivative gain, and torque gain, respectively.

Two velocity compensators C_{vs} and C_{vc} (Fig. 3) were designed such that the two motors have the same damping coefficient. The description of the velocity compensator is

$$C_{vs} = \left(\nu - \frac{B_{sn}}{J_{sn}}\right)s, \quad C_{vc} = \left(\nu - \frac{B_{cn}}{J_{cn}}\right)s, \times \left[\nu = \max\left(\frac{B_{sn}}{J_{sn}}, \frac{B_{cn}}{J_{cn}}\right)\right]. \tag{15}$$

With the velocity compensators, the two motors have the same damping coefficient, which means that the transfer function from u_{xi} to θ_i is

$$\Theta_i = \frac{1}{s^2 + B_x s} U_{xi}, \qquad B_x = \max\left(\frac{B_{sn}}{J_{sn}}, \frac{B_{cn}}{J_{cn}}\right). \tag{16}$$

4 Design and Analysis

4.1 *Detailed Design*

Stability is the most important and basic requirement for the overall system. The controller is designed on the basis of the small gain theorem to guarantee system stability.

4.1.1 *Two-loop disturbance observer*

A two-loop DOB was employed as the internal loop robust compensator (Fig. 4). The robust compensator is composed of two DOBs.[22] The external disturbance D_i and model uncertainty $\Delta_i(s)$ are mainly compensated for by the internal DOB. According to Fig. 4, the transfer function from U_i' to Θ_i and the transfer function from D_i to Θ_i are Eqs. (17) and (18), respectively,

$$\frac{\Theta_i}{U_i'} = \frac{G_i(s)G_{in}(s)}{G_{in}(s)[1 - Q(s)] + G_i(s)Q(s)}, \tag{17}$$

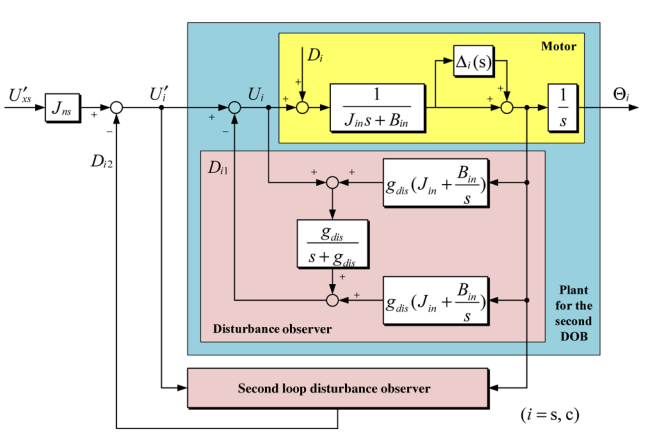

Fig. 4 Two-loop DOB to guarantee that the dynamic characteristics of a motor are the same as those of the nominal model, which is useful for improving the practical performance of the proposed compensation method.

$$\frac{\Theta_i}{D_i} = \frac{G_i(s)G_{in}(s)[1 - Q(s)]}{G_{in}(s)[1 - Q(s)] + G_i(s)Q(s)}, \tag{18}$$

$$G_{in}(s) = \frac{1}{J_{in}s^2 + B_{in}s}, \qquad Q(s) = \frac{g_{dis}}{s + g_{dis}}. \tag{19}$$

If the cutoff frequency g_{dis} is infinity, the transfer function from U_i' to Θ_i and that from D_i to Θ_i become $G_{in}(s)$ and 0, respectively. This means that the DOB completely compensates for the disturbance and uncertainty. However, to guarantee system stability, g_{dis} should not be infinity.[23] The complementary sensitivity function of the motor with DOB is

$$T(s) = Q(s) = \frac{g_{dis}}{s + g_{dis}}. \tag{20}$$

According to the small gain theorem,[24] a motor with DOB is stable if

$$\left\| \frac{g_{dis}}{s + g_{dis}} \Delta_i(s) \right\|_\infty < 1. \tag{21}$$

To reduce the conservation, a parameter is designed on the basis of measured characteristics of the uncertainty $\Delta_i(s)$. We obtained the dynamic characteristics of the motor in the frequency domain by choosing a pseudo white noise as the input value $u_i(t)$ and using a spectral analysis based on the fast Fourier transform (FFT). Then, the model uncertainty $\Delta_i(s)$ could be calculated and plotted.

Figure 5(a) shows the real dynamic characteristics and the nominal model of the scan motor in the imaging system. On the basis of this data, the cutoff frequency was designed subject to the condition in Eq. (21). Figure 5(b) shows the magnitude–frequency characteristics of $[g_{dis}/(s + g_{dis})]\Delta_s(s)$. In this system, the parameter g_{dis} was designed as $g_{dis} = 300$ rad/s using trial and error by suppressing the curve of $|[g_{dis}/(j\omega + g_{dis})]\Delta_s(j\omega)|$ under 0 dB with some

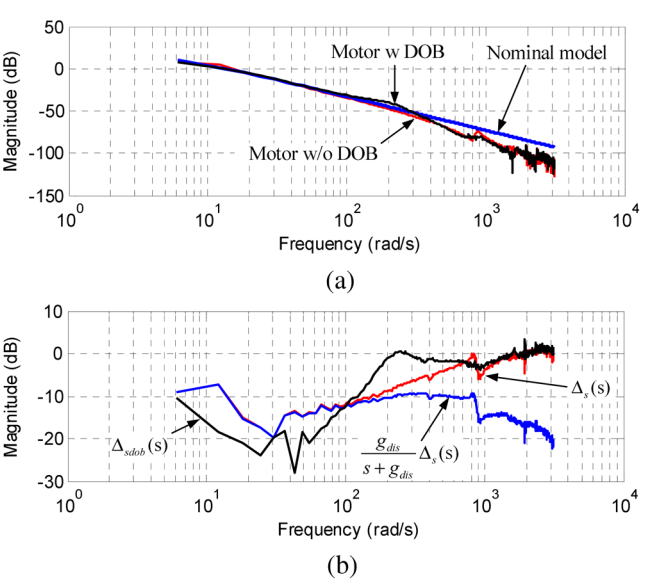

Fig. 5 Magnitude–frequency characteristics: (a) identified real motor, nominal model, and real motor with DOB; and (b) uncertainties and stability criterion.

margins. According to Fig. 5(b), the condition in Eq. (21) is met, i.e., the motor with the internal loop DOB is stable.

However, because of the limited g_{dis}, residual disturbance and model uncertainty still exist in the system, although the DOB compensates for most of the external disturbance and model uncertainty. Figure 5 also shows the dynamic characteristics of the motor with the internal DOB. Such a system can also be described by the nominal model and an uncertainty as

$$G_{idob}(s) = G_{in}(s)[1 + \Delta_{idob}(s)] \qquad (i = s, c). \tag{22}$$

A comparison of $\Delta_{sdob}(s)$ and $\Delta_s(s)$ in Fig. 5 reveals that the difference between the nominal model and the real motor is reduced at low frequencies. However, the difference is still not zero. To further reduce the model uncertainty, a second loop DOB was designed (Fig. 4). This second loop DOB was the same as the internal one. An added parameter $\alpha(\alpha \le 1)$ was employed to tune the complementary sensitivity function. The stability condition of the second DOB is

$$\left\| \alpha \frac{g_{dis}}{s + g_{dis}} \Delta_{idob}(s) \right\|_\infty < 1. \tag{23}$$

By a similar process, the parameter of α was designed using the magnitude–frequency characteristics of $\Delta_{idob}(s)$.

Remark. The additional parameter α reduces the H_∞ norm in Eq. (23), and also reduces the effect of model uncertainty rejection. This parameter should be close to 1. In practice, an iteration method can be employed to design this parameter.

The design processes for the two robots are completely identical.

The estimated disturbance δ_i equals $D_{i1} + D_{i2}$ according to Figs. 3 and 4. In Fig. 4, the transfer function from U_{xi} to Θ_i is

$$G'_{in}(s)\left(\frac{1}{s^2 + B_x s}\right)[1 + \Delta'_i(s)] \qquad (i = s, c), \tag{24}$$

where $\Delta'_i(s)$ is the residual uncertainty of the motor with the two-loop DOB.

The two-loop DOB, i.e., the robust compensator, minimizes the difference in the dynamic characteristics between the two motors.

4.1.2 *Bilateral controller*

The position and scan controllers in the bilateral control algorithm were designed on the basis of the concept of modal transformation[25] and small gain theorem. The dynamics of the bilateral control system is expressed as

$$\Theta_s = G'_{sn}(s)[C_p(s)(\Theta_c - \Theta_s) + C_t(T_s + T_c)], \tag{25}$$

$$\Theta_c = G'_{cn}(s)[C_p(s)(\Theta_s - \Theta_c) + C_t(T_s + T_c)]. \tag{26}$$

Assume that $G'_{sn}(s) = G'_{cn}(s)[1 + \Delta_{sc}(s)]$. Then subtracting Eq. (25) by Eq. (26) yields

$$\begin{aligned}\Theta_s - \Theta_c &= G'_{cn}(s)C_p(s)(\Theta_c - \Theta_s)[2 + \Delta_{sc}(s)] \\ &\quad + G'_{cn}(s)\Delta_{sc}(s)C_t(T_s + T_c) \\ &= \frac{2}{s^2 + B_x s}[1 + \Delta_x(s)]C_p(s)[0 - (\Theta_s - \Theta_c)] + D_d,\end{aligned} \tag{27}$$

$$\Delta_x(s) = \Delta_c(s) + \frac{\Delta_{sc}(s)}{2} + \frac{\Delta_{sc}(s)\Delta_c(s)}{2}, \tag{28}$$

$$D_d = \Delta_a(s)C_tC_s(s)(2\Theta - \Theta_s - \Theta_c), \tag{29}$$

$$\Delta_a(s) = G'_{sn}(s) - G'_{cn}(s). \tag{30}$$

Equation (27) is a feedback system with the nominal model $2/(s^2 + B_x s)$, controller $C_p(s)$, and disturbance D_d (Fig. 6). According to the small gain theorem, the system is stable if Eq. (31) is satisfied

$$\left\| \frac{2C_p(s)}{s^2 + B_x s + 2C_p(s)} \Delta_x(s) \right\|_\infty < 1. \tag{31}$$

Similarly, adding Eqs. (25) and (26) yields

$$\begin{aligned}&\Theta_s + \Theta_c \\ &\quad = \frac{2}{s^2 + B_x s}[1 + \Delta_x(s)]C_tC_s(s)[2\Theta - (\Theta_s + \Theta_c)] + D_a,\end{aligned} \tag{32}$$

$$D_a = 2\Delta_a(s)C_p(s)(\Theta_c - \Theta_s). \tag{33}$$

Equation (32) is also a feedback system with the nominal model $2/(s^2 + B_x s)$, controller $C_tC_s(s)$, and disturbance D_a (Fig. 7). According to the small gain theorem, the system is stable if Eq. (34) is satisfied

$$\left\| \frac{2C_tC_s(s)}{s^2 + B_x s + 2C_tC_s(s)} \Delta_x(s) \right\|_\infty < 1. \tag{34}$$

According to Eqs. (28), (31), and (34), the gains in the position controller $C_p(s)$, torque controller C_t, and scan controller $C_s(s)$ are restricted by the model uncertainties of each motor and the difference between the two motors.

Figure 8 shows the magnitude–frequency characteristics of the uncertainty $\Delta_x(s)$ and the H_∞ norm in Eqs. (31) and (34) with the controllers in Eq. (35). The parameters of the

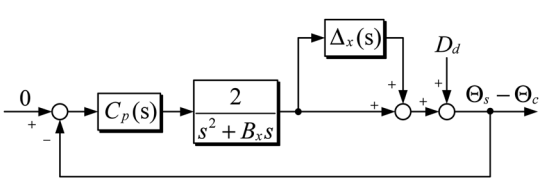

Fig. 6 Feedback loop for designing the position controller in bilateral control framework.

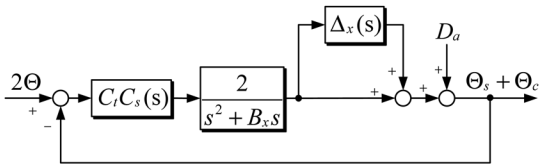

Fig. 7 Feedback loop for designing the scan controller and torque controller in bilateral control framework.

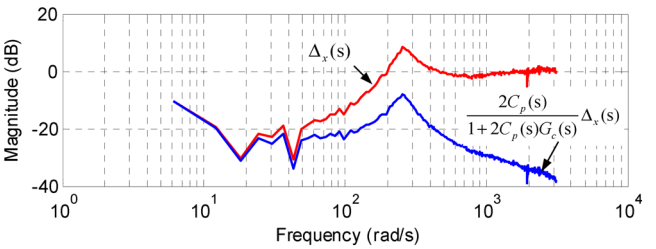

Fig. 8 Magnitude–frequency characteristics of the equivalent uncertainty and stability criterion of the controller design.

controllers are tuned by trial and error to guarantee system stability with a margin better than −10 dB

$$C_p(s) = C_s(s) = 200 + 20s, \qquad C_t = 1. \tag{35}$$

4.2 *Performance Analysis*

The feedback loops shown in Figs. 6 and 7 are also useful for analyzing the system performance. Assume that the controllers still have the relationship of Eq. (35). According to Eq. (27), the tracking error between the two motors is only related to D_d that is a weighted control torque of scan.

Substituting Eqs. (29), (32), and (33) into Eq. (27) gives

$$\Theta_s - \Theta_c = \frac{\Delta_a(s)C_p(s)}{1 + G(s)C_p(s)}(2\Theta - \Theta_s - \Theta_c), \tag{36}$$

$$G(s) = \frac{2}{s^2 + B_x s}[1 + \Delta_x(s)]. \tag{37}$$

Then, substituting Eqs. (36) and (33) into Eq. (32) gives

$$2\Theta - \Theta_s - \Theta_c = \frac{2}{1 + G(s)C_p(s)}\Theta + \frac{2\Delta_a(s)C_p(s)}{1 + G(s)C_p(s)}(\Theta_s - \Theta_c). \tag{38}$$

By combining Eqs. (36) and (38), the following equations are obtained:

$$\Theta_s - \Theta_c = \frac{2\Delta_a(s)C_p(s)}{[1 + G(s)C_p(s)]^2 - 2\Delta_a^2(s)C_p^2(s)}\Theta, \tag{39}$$

$$\Theta - \frac{\Theta_s + \Theta_c}{2} = \frac{1 + G(s)C_p(s)}{[1 + G(s)C_p(s)]^2 - 2\Delta_a^2(s)C_p^2(s)}\Theta. \tag{40}$$

According to Eq. (39), the position error between the two motors is mainly governed by uncertainty $\Delta_a(s)$, controller $C_p(s)$, and command Θ.

In particular, the error converges to zero when the command is zero or the uncertainty $\Delta_a(s) = 0$.

If the difference between the two motors is sufficiently small, satisfactory tracking between the two robots is also achieved. Increasing the gain of $C_p(s)$ can increase the magnitude of the denominator of Eq. (39) at certain frequencies. However, it also increases the numerator of Eq. (39). Therefore, the effect of decreasing the model uncertainty is better than the effect of simply increasing the gain of $C_p(s)$.

According to Eq. (40), the tracking error between the whole bilateral control system and the scan command is mainly governed by $C_p(s)$. If the uncertainty $\Delta_a(s) = 0$, the transfer function of scan control error is completely identical to that of a single tracking system with single motor. Therefore, the bilateral control hardly influences the performance of the scan control. This means that the proposed method is a feasible method for updating the traditional scan imaging systems.

Similar to the stability constraint, the performance can also be expressed using the H_∞ norm. To achieve better performance,

$$\min \left\| \begin{matrix} \frac{2\Delta_a(s)C_p(s)}{[1+G(s)C_p(s)]^2-2\Delta_a^2(s)C_p^2(s)} \\ \frac{1+G(s)C_p(s)}{[1+G(s)C_p(s)]^2-2\Delta_a^2(s)C_p^2(s)} \end{matrix} \right\|_\infty \tag{41}$$

should be obtained. Assume that W_Θ is the weighting function of Θ. The overall system is expressed as a standard H_∞ optimization problem

$$\left\| \begin{matrix} \frac{2\Delta_a(s)C_p(s)}{[1+G(s)C_p(s)]^2-2\Delta_a^2(s)C_p^2(s)} W_\Theta \\ \frac{1+G(s)C_p(s)}{[1+G(s)C_p(s)]^2-2\Delta_a^2(s)C_p^2(s)} W_\Theta \\ \frac{2C_p(s)}{s^2+B_xs+2C_p(s)}\Delta_x(s) \\ \frac{2C_tC_s(s)}{s^2+B_xs+2C_tC_s(s)}(s)\Delta_x(s) \end{matrix} \right\|_\infty < 1. \tag{42}$$

The controller in this study may be replaced by other designs with a more general form. For example, a lead–lag compensator may be used. More general H_∞ controllers are also feasible designs by solving Riccati equations based on a state-space formulation. However, it is quite difficult to directly calculate the controller using Eq. (42), because the transfer functions in the H_∞ norm are too complex. In engineering, constraints can be employed to verify simple controllers.

In practice, Eqs. (39) and (40) for verifying the performance of the proposed method are implemented by a plotting method. Figure 9 shows the magnitude–frequency characteristics of the transfer functions in Eqs. (39) and (40). According to Fig. 9, the magnitude of the transfer function from Θ to $\Theta_s - \Theta_c$ is suppressed under −60 dB. This result means that the position error between the two motors is smaller than 0.001Θ.

Remark. The plotting was implemented using the data of spectral analysis. Therefore, the accuracy of this performance analysis was also governed by the spectral analysis. In this study, FFT with the Hanning windowing function was employed as the spectral analysis tool. The choice of the windowing function influences the quality of information

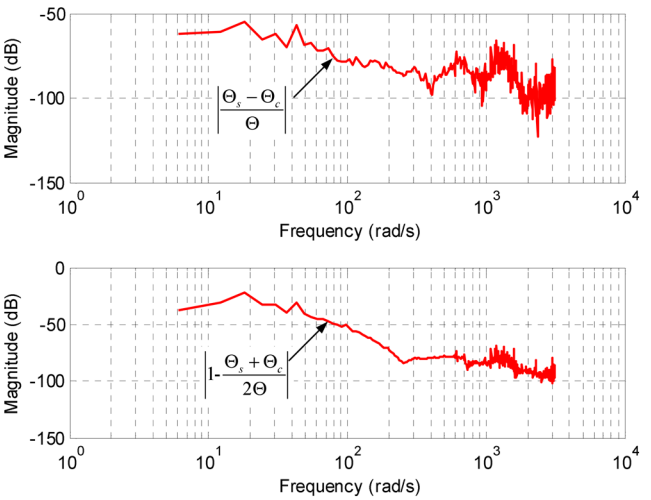

Fig. 9 Magnitude–frequency characteristics of transfer functions for performance analysis.

obtained by model uncertainty analysis. In engineering practice, the Hanning windowing function has satisfactory accuracy and effect of noise suppression. Engineers can perform this analysis by programming in a digital signal processor or directly using a spectrum analyzer.

5 Experiments

5.1 *Experimental Setup*

Figure 10 shows the experimental setup. Two brushless motors were employed, one as the scan motor and the other as the compensation motor. The focus distance of the lens was 35 mm. The imaging detector was a CMOS camera. The position responses of the motors were measured using an optical-electricity encoder with a resolution of 0.00007 deg. The required differential calculation was performed by the nonlinear tracking differentiator in Ref. 26. The overall algorithms were implemented on a computer by programming in Linux-RTAI, which is a real-time operating system.[27,28] The sampling time was 1 ms. Other parameters in the proposed control algorithm are listed in Table 1.

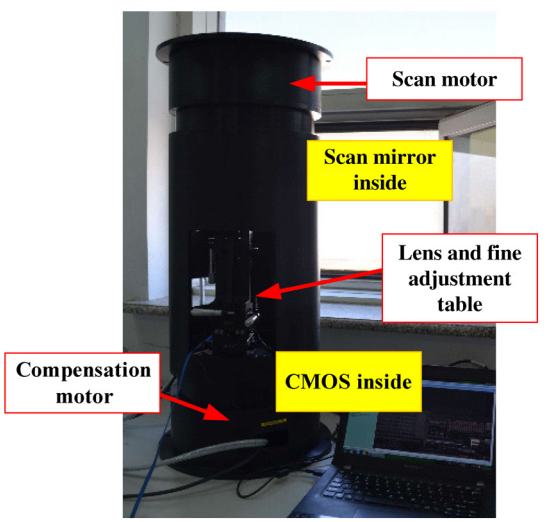

Fig. 10 Experimental setup.

Table 1 Experimental parameters.

Parameter	Notation	Value
Scan motor's nominal inertia (kg m^2)	J_{sn}	0.004347826
Scan motor's nominal damping coefficient (s^{-1})	B_{sn}	0.04347826
Compen. motor's nominal inertia (kg m^2)	J_{cn}	0.003125
Compen. motor's nominal damping coefficient (s^{-1})	B_{cn}	0.03125
Position control gain (s^{-2})	K_P	200.0
Velocity control gain (s^{-1})	K_D	20.0
Torque control gain [(kg m^2)$^{-1}$]	K_t	1.0
DOB cutoff frequency (rad/s)	g_{dis}	300.0
Weighting of second DOB	α	0.5
Damping coefficient compensation (s^{-1})	ν	10.0

The parameters were tuned by the design method described in Sec. 4.

For comparison, a traditional unilateral tracking method, described by Eqs. (43) and (44), was also implemented with the parameters listed in Table 1. The traditional unilateral method does not have torque control channels but only tracking control in a single direction

$$U_{xs} = (K_P + K_D s)(\Theta - \Theta_s), \tag{43}$$

$$U_{xc} = (K_P + K_D s)(\Theta_s - \Theta_c). \tag{44}$$

In the experiments, the scalar valued norm of the tracking error between the two motors was used as a measure of average tracking performance

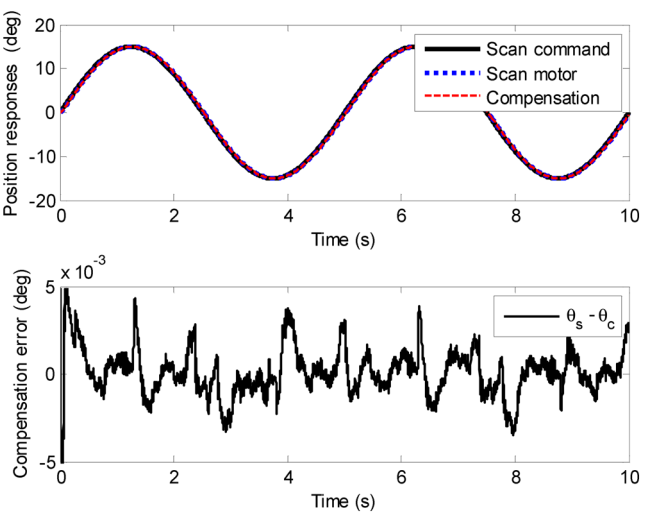

Fig. 11 Position responses of the scan motor and compensation motor with the proposed bilateral control-based compensation.

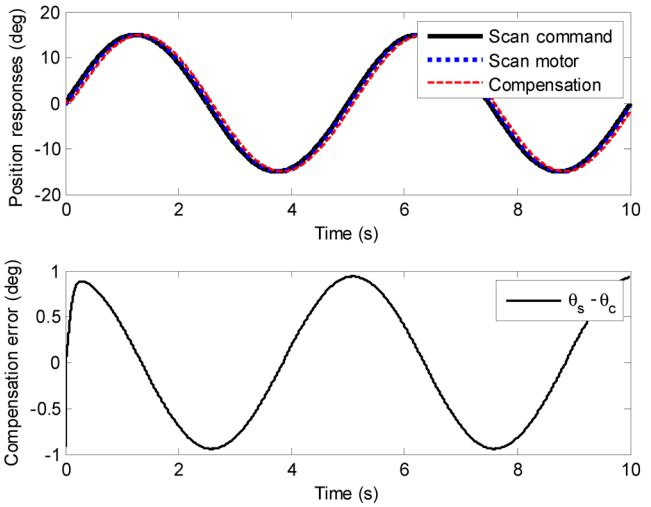

Fig. 12 Position responses of the scan motor and compensation motor with traditional unilateral tracking control.

$$L_2(e) = \sqrt{\frac{1}{T_f}\int_0^{T_f} |\theta_s(\tau) - \theta_c(\tau)|^2 \mathrm{d}\tau}, \tag{45}$$

where T_f represents the running time. T_f was selected as double periods of the scan command $15\sin(2\pi 0.2t)$ (deg). Such a scan command tests the system with a scan speed from 0 to 19 deg/s. This range of speed and the period of the scan movement are commonly used in engineering practice.

5.2 *Experimental Results*

Figure 11 shows the experimental results of the position responses when the proposed method was implemented. The method successfully achieves synchronous responses between the two motors, which is highly consistent with the design and analysis. In the experiment, the largest absolute value of the compensation error was 4.2×10^{-3} deg, and $L_2(e)$ was 1.1207×10^{-3} deg. The size and dimensions of the pixel in the CMOS camera were 5.3 μm and 1280×1024, respectively. Therefore, the largest displacement in the scanned photograph was less than 0.32 μm, which is only 6% of the pixel size. Therefore, the bilateral control-based compensation method achieves satisfactory results.

Figure 12 shows the experimental results of the position responses with the traditional unilateral tracking control. Compared with the results in Fig. 11, with the same control

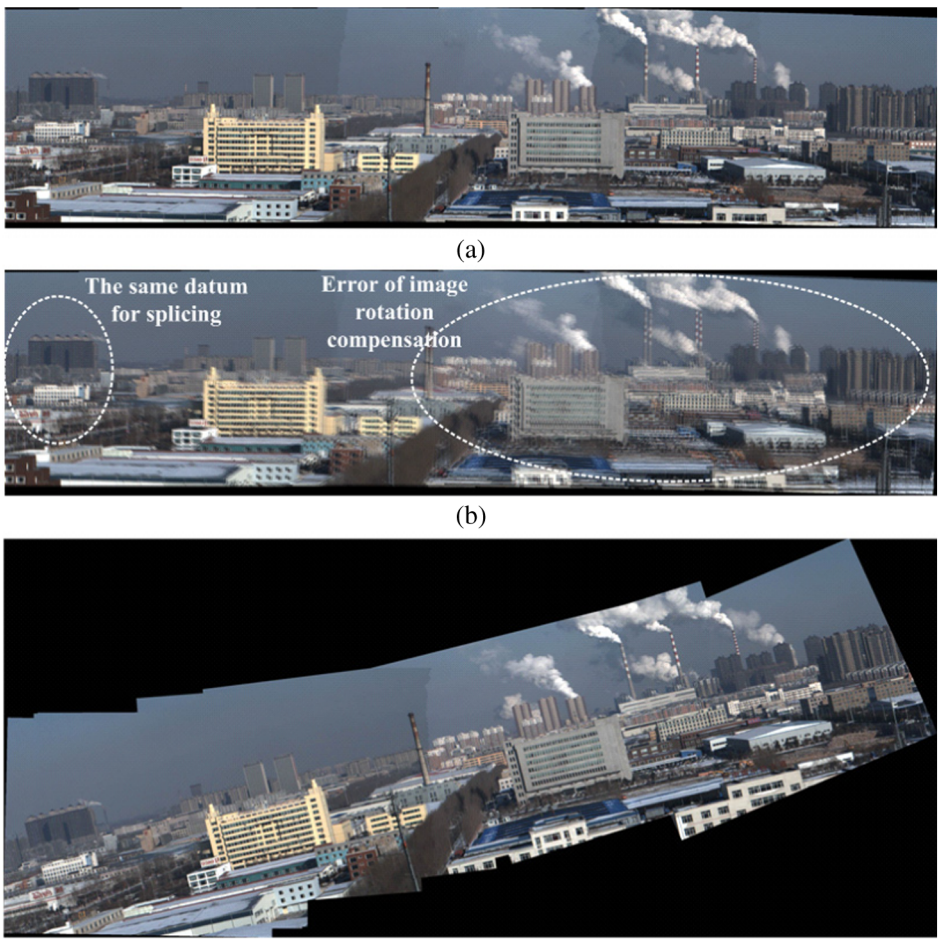

Fig. 13 Spliced photographs using image rotation compensation: (a) result achieved using the proposed bilateral control-based compensation; (b) superposed photograph composed of the result achieved using the proposed method and that using traditional unilateral tracking control; and (c) result without any compensation.

parameters, the tracking error between the two motors is markedly larger. The peak absolute value of the error was 0.95 deg, and $L_2(e)$ was 0.6649 deg, which is 593 times greater than the corresponding result achieved using the proposed method. The largest displacement in the scanned photograph was 72 μm, which does not quite satisfy the requirements of accurate imaging.

Figure 13 shows the spliced photographs in the experiments. With the proposed method, a clear panoramic photograph that contains accurate geographic position information was achieved [Fig. 13(a)]. Figure 13(b) shows the result of superposing the photograph with the proposed method and the photograph with the traditional unilateral tracking. The two photographs have the same datum for splicing on the left side. Because of the compensation error, a marked deviation occurs on the right side in the position of scenery with the traditional compensation control, compared with the result achieved using the proposed method.

Figure 13(c) shows the result achieved without any compensation for the rotation in imaging. To realize splicing, a series of photographs must be rotated in the reverse direction, which results in a loss of information. Moreover, the position information of the object in the photograph would not be correct.

In summary, the proposed method provides a satisfactory effect of compensating for the rotation in imaging. Compared with the traditional unilateral tracking compensation, the proposed method reduces the L_2 norm of the synchronous error by 99.83%. The proposed approach yields a better photograph that contains accurate position information of the scenery.

6 Conclusion

This paper considered the problem of rotation in imaging in scan imaging systems. A method of compensation for the rotation in imaging was proposed on the basis of the concept of bilateral control derived from the field of haptic teleoperation.

The proposal does not involve changing the hardware of a scan imaging system. It establishes four interactive channels of information between the scan motor and the compensation motor, namely, two channels of position information and two channels of torque information. Based on the idea of bilateral control algorithm, the proposal improves the synchronism between the two motors. The stability and performance of the proposal are analyzed based on a group of H_∞ norms.

Experiments were carried out to validate the proposed control method. The algorithm was realized by programming in a real-time computer system. The experimental results showed a reduction of over 99% in the compensation error, which validated the proposed method. Photographs that contain more accurate information of the scenery can be achieved by applying the proposed method. The relatively high requirements of photogrammetry and many other industrial applications can also be satisfied.

As future research, a bilateral control system using a more complex model structure for the motors can be designed and analyzed. Furthermore, a more general controller structure can be derived from a state-space formulation of the control problem.

Acknowledgments

This study was supported in part by the National Science Foundation of China under Grant No. 61304032, and in part by the CIOMP Knowledge Innovation Program under Grant Nos. Y3CX1SS149 and Y4CX1SS146.

References

1. J. Kyoung et al., "Epsilon-near-zero meta-lens for high resolution wide-field imaging," *Opt. Express* **22**(26), 31875–31883 (2014).
2. M. S. Akselrod et al., "FNTD radiation dosimetry system enhanced with dual-color wide-field imaging," *Radiat. Meas.* **71**, 166–173 (2014).
3. J. Xie et al., "Real-time adjustment of optical transmitter by laser beam parameter measurement based on two linear array CCD scanning imaging," *Optik* **125**(15), 3991–3995 (2014).
4. Y. Yoon et al., "Robust scanning scheme over large area for airborne EO/IR camera," *Proc. SPIE* **8185**, 81850X (2011).
5. S. Mende, "Auroral imaging from a spinning satellite," *Rev. Sci. Instrum.* **82**(1), 013102 (2011).
6. C. Yu et al., "Analysis of image rotation for aerial remote sensor with off-axis three-reflective optical system," in *2012 Int. Conf. on Applied Physics and Industrial Engineering*, pp. 225–232 (2012).
7. T. Zheng et al., "Image rotation measurement in scene matching based on holographic optical correlator," *Appl. Opt.* **52**(12), 2841–2848 (2013).
8. W. Wei et al., "Estimation of image rotation angle using interpolation-related spectral signatures with application to blind detection of image forgery," *IEEE Trans. Inf. Forensics Secur.* **5**(3), 507–517 (2010).
9. T. Zheng et al., "Full-range in-plane rotation measurement for image recognition with hybrid digital-optical correlator," *Opt. Eng.* **53**(1), 011003 (2014).
10. J. Xiong et al., "Non-mechanical programmable image rotator with Glan–Thompson prism," *Proc. SPIE* **5557**, 124–131 (2004).
11. R. Davies et al., "MICADO: the E-ELT adaptive optics imaging camera," *Proc. SPIE* **7735**, 77352A (2010).
12. M. K. Masten, "Inertially stabilized platforms for optical imaging systems—tracking dynamic targets with mobile sensors," *IEEE Control Syst.* **28**(1), 47–64 (2008).
13. T. Tang et al., "Compensating for some errors related to time delay in a charge-coupled-device-based fast steering mirror control system using a feedforward loop," *Opt. Eng.* **49**(7), 073005 (2010).
14. L. Shen et al., "Rate control based on an incremental proportional–integral–differential algorithm," *Opt. Eng.* **46**(7), 077002 (2007).
15. R. Wirz et al., "Bidirectional transport protocol for teleoperated robots," *IEEE Trans. Ind. Electron.* **56**(9), 3772–3781 (2009).
16. D. A. Lawrence, "Stability and transparency in bilateral teleoperation," *IEEE Trans. Rob. Autom.* **9**(5), 624–637 (1993).
17. Y. Sumiyoshi and K. Ohnishi, "The transformation of modified 4-channel architecture," in *8th IEEE Int. Workshop on Advanced Motion Control*, pp. 211–216 (2004).
18. A. Mohammadi, M. Tavakoli, and H. J. Marquez, "Disturbance observer-based control of non-linear haptic teleoperation systems," *IET Control Theory Appl.* **5**(18), 2063–2074 (2011).
19. A. Vafaei and M. J. Yazdanpanah, "Terminal sliding mode impedance control for bilateral teleoperation under unknown constant time delay and uncertainties," in *2013 European Control Conf.*, pp. 3748–3753 (2013).
20. C. Mitsantisuk, K. Ohishi, and S. Katsura, "Estimation of action/reaction force for the bilateral control using Kalman filter," *IEEE Trans. Ind. Electron.* **59**(11), 4383–4393 (2012).
21. P. Mouroulis and J. Macdonald, *Geometrical Optics and Optical Design*, Oxford University Press, Oxford, United Kingdom (1997).
22. K. Ohnishi, M. Shibata, and T. Murakami, "Motion control for advanced mechatronics," *IEEE/ASME Trans. Mechatron.* **1**(1), 56–67 (1996).
23. E. Sariyildiz and K. Ohnishi, "Stability and robustness of disturbance-observer-based motion control systems," *IEEE Trans. Ind. Electron.* **62**(1), 414–422 (2015).
24. K. Zhou, *Essentials of Robust Control*, Prentice Hall, Upper Saddle River, New Jersey (1999).
25. S. Katsura and K. Ohishi, "Modal system design of multirobot systems by interaction mode control," *IEEE Trans. Ind. Electron.* **54**(6), 1537–1546 (2007).
26. D. Tian, H. Shen, and M. Dai, "Improving the rapidity of nonlinear tracking differentiator via feedforward," *IEEE Trans. Ind. Electron.* **61**(7), 3736–3743 (2014).
27. M. Chiandone et al., "Industrial motion control applications using Linux RTAI," in *Int. Symp. on Power Electronics, Electrical Drives, Automation and Motion*, pp. 528–533 (2008).
28. A. Barbalace et al., "Performance comparison of Vxworks, Linux, RTAI, and Xenomai in a hard real-time application," *IEEE Trans. Nucl. Sci.* **54**(1), 435–439 (2008).

Dapeng Tian received his BE degree from Beijing Institute of Technology, China, in 2007. He was received his PhD at Beihang University, China, in 2012. From 2009 to 2011, he was with the Advanced Research Center, Keio University, Yokohama, Japan, as a co-researcher. Since 2012, he has been with the Key Laboratory of Airborne Optical Imaging and Measurement, Changchun Institute of Optics, Fine Mechanics and Physics, Chinese Academy of Sciences, China. His current research interests include optical imaging, motion control theory, and engineering.

Yutang Wang received her BE and MS degrees from Beijing Institute of Technology, in 2009 and 2012, respectively. Now she is currently with Key Laboratory of Airborne Optical Imaging and Measurement, Changchun Institute of Optics, Fine Mechanics and Physics, Chinese Academy of Sciences. Her main research interest is servo control.

Fuchao Wang received his BE and MS degrees from Harbin Engineering University, in 2011 and 2013, respectively. He is currently with Key Laboratory of Airborne Optical Imaging and Measurement, Changchun Institute of Optics, Fine Mechanics and Physics, Chinese Academy of Sciences. His current area of interest is real-time control systems.

Yupeng Zhang received his BE and MS degrees from Jilin University, China, in 2009 and 2012, respectively. From 2012, he was with Changchun Institute of Optics, Fine Mechanics and Physics, Chinese Academy of Sciences. His current research is design and optimization of optoelectronic platform.